Electron interaction and spin effects in quantum wires, quantum dots and quantum point contacts: a first-principles mean-field approach

2008 J. Phys.: Condens. Matter 20 164217

(http://iopscience.iop.org/0953-8984/20/16/164217)

IOP PUBLISHING JOURNAL OF PHYSICS: CONDENSED MATTER

J. Phys.: Condens. Matter **20** (2008) 164217 (17pp) doi:10.1088/0953-8984/20/16/164217

Electron interaction and spin effects in quantum wires, quantum dots and quantum point contacts: a first-principles mean-field approach

I V Zozoulenko and S Ihnatsenka

Solid State Electronics, Department of Science and Technology (ITN), Linköping University, 60174 Norrköping, Sweden

Received 5 October 2007, in final form 14 November 2007
Published 1 April 2008
Online at stacks.iop.org/JPhysCM/20/164217

Abstract

We have developed a mean-field first-principles approach for studying electronic and transport properties of low dimensional lateral structures in the integer quantum Hall regime. The electron interactions and spin effects are included within the spin density functional theory in the local density approximation where the conductance, the density, the effective potentials and the band structure are calculated on the basis of the Green's function technique. In this paper we present a systematic review of the major results obtained on the energetics, spin polarization, effective g factor, magnetosubband and edge state structure of split-gate and cleaved-edge overgrown quantum wires as well as on the conductance of quantum point contacts (QPCs) and open quantum dots. In particular, we discuss how the spin-resolved subband structure, the current densities, the confining potentials, as well as the spin polarization of the electron and current densities in quantum wires and antidots evolve when an applied magnetic field varies. We also discuss the role of the electron interaction and spin effects in the conductance of open systems focusing our attention on the 0.7 conductance anomaly in the QPCs. Special emphasis is given to the effect of the electron interaction on the conductance oscillations and their statistics in open quantum dots as well as to interpretation of the related experiments on the ultralow temperature saturation of the coherence time in open dots.

(Some figures in this article are in colour only in the electronic version)

1. Introduction

Electron–electron interaction is known to have a great impact on electronic and transport properties of low dimensional structures such as quantum wires, quantum point contacts, quantum dots and antidots. This includes such pronounced examples as Coulomb blockade [1] and Kondo effect [2] in quantum dots, exchange enhancement of the g-factor [3] and a spatial spin separation on wire edges in the quantum Hall regime [4], the '0.7-anomaly' in quantum point contacts [5] and many others.

Theoretical description of electron interactions in the above systems can be performed from many different standpoints, including field-theoretical approaches, exact numerical techniques, perturbation methods, mean-field theories etc. Very often this description is based on model Hamiltonians containing phenomenological parameters of the theory such as coupling strengths or charging constants. In many cases it is not always straightforward to relate quantitatively the above parameters to the physical processes they represent in the real system and sometimes it is not even obvious whether a model description is sufficient to capture the essential physics. At the same time, it is now well recognized that a detailed understanding and interpretation of experiments might require quantitative microscopical modeling of the system at hand, free from phenomenological parameters and not relying on model Hamiltonians which validity is poorly controlled. The importance of such modeling can be illustrated by examples including the quantitative description of the compressible and/or incompressible strips in magnetic field

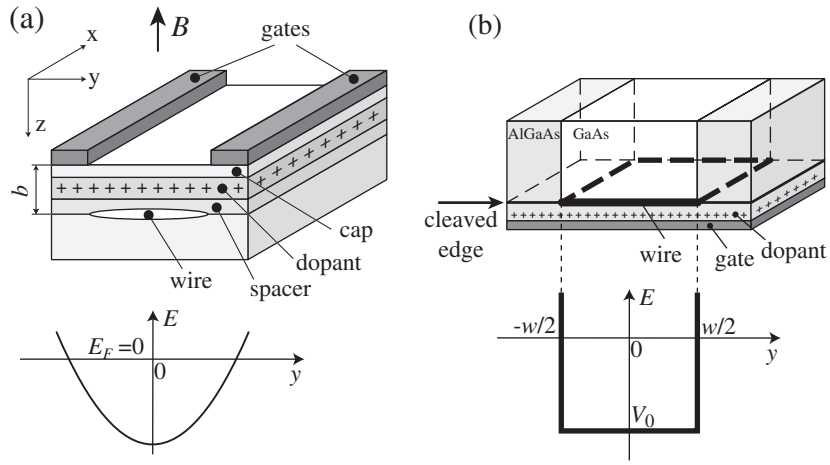

Figure 1. Schematic geometries and bare confining potentials (upper and lower panels respectively) for (a) a split-gate quantum wire and (b) a cleaved-edge overgrown quantum wire. For the case of the split-gate wire the bare confining potential $V_{\rm conf}(y)$ is well approximated by the parabolic confinement with $V_0 = -85$ meV, $\hbar\omega_c = 2$ meV. With these parameters the local (sheet) density in the wire center $n = 1.5 \times 10^{15}$ m^{-2} and the effective width of the wire $w \approx 400$ nm. For the case of the cleaved-edge wire, the bottom of the confinement potential $V_0 = -0.1$ eV, and the wire width $w = 300$ nm. This corresponds to the sheet electron density in the wire center $n_{2D} \approx 1.5 \times 10^{15}$ m^{-2}. For both wires the distance between the 2DEG and the surface $b = 60$ nm, temperature $T = 1$ K, $E_{\rm F} = 0$.

at the edges of the two-dimensional electron gas [6] or explanation of the Hund rule observed in few-electron quantum dots [7], just to name a few examples.

One of the most powerful approaches capable of providing detailed microscopical information on the system at hand is the mean-field approach, such as the density functional theory (DFT) or the Hartree–Fock theory (HF) [8]. In these methods, each particle moves in the effective interaction potential generated by the rest of the particles. The strength of the mean-field approaches is that they can provide detailed microscopic information about electron densities, wavefunctions, potentials, etc (which is not possible within field-theoretical approaches that typically rely on model Hamiltonians and phenomenological parameters of the theory). At the same time, the mean-field approaches can deal with large realistic systems containing hundreds or thousands of electrons. Such systems would be forbiddingly large for the exact methods such as quantum Monte Carlo or configurational integration.

We have recently applied the mean-field approaches to study electronic and transport properties of various low dimensional lateral structures, including quantum wires, quantum antidots, quantum point contacts and open quantum dots [11–19]. The developed approaches correspond to the first-principles magnetoconductance calculations (within the effective mass approximation), that start from a geometrical layout of the device, are free from phenomenological parameters and do not rely on model Hamiltonians whose validity is poorly controlled. In the present paper we provide a systematic review of the major obtained results. The paper is organized as follows. A brief presentation of electronic structure calculations for quantum wires in the integer quantum Hall regime is given in section 2.1. section 2.2 describes energetics of the split-gate quantum wire including magnetosubband structure and spin polarizations, spin-resolved edge state structure, effect of the external confinement and others. In this section we also compare the results obtained within the spin-DFT with those calculated on the basis of the Hartree–Fock theory, as well as compare the edge state structure in quantum wires and in quantum antidots. The energetics of cleaved-edge overgrown quantum wire is described in section 2.3. Section 3 is devoted to conductance of open systems such as quantum point contacts and open quantum dots. In the concluding section we summarize obtained results, discuss limitations of the developed approaches as well as provide an outline for the future research.

2. Quantum wires in the integer quantum Hall regime

2.1. Model and method

We study an infinitely long quantum wire in a perpendicular magnetic field B. We consider two types of confinements, a split-gate quantum wire (figure 1(a)), and a cleaved-edge overgrown quantum wire (figure 1(b)). The Hamiltonian reads, $H = \sum_\sigma (H_0 + V^\sigma(y))$, where H_0 is the kinetic energy in the Landau gage, $H_0 = -\frac{\hbar^2}{2m^*}\{(\frac{\partial}{\partial x} - \frac{eiBy}{\hbar})^2 + \frac{\partial^2}{\partial y^2}\}$, and $V^\sigma(y)$ is the total confinement potential [11–13, 15, 19],

$$V^\sigma(y) = V_{\rm conf}(y) + V^\sigma_{\rm eff}(y) + g\mu_b B\sigma, \qquad (1)$$

$\sigma = \pm\frac{1}{2}$ describes spin-up and spin-down states, $\uparrow$, $\downarrow$, and $m^* = 0.067m_{\rm e}$ is the GaAs effective mass. The last term in equation (1) accounts for Zeeman energy where $\mu_b = {\rm e}\hbar/2m_{\rm e}$ is the Bohr magneton, and the bulk g factor of GaAs is $g = -0.44$. In the split-gate geometry the confining potential $V_{\rm conf}(y)$ is given by the electrostatic potential from the gates, donor layers and the Schottky barrier (the corresponding analytical expressions for these potential can be found in [9, 10]; the Schottky barrier is chosen to

be $V_{\text{Schottky}} = 0.8$ eV). The analytic expression for $V_{\text{conf}}(y)$ for the split-gate wire is well approximated by the parabolic confinement, $V_{\text{conf}}(y) = V_0 + \frac{m^*}{2}(\omega_0 y)^2$, where V_0 defines the bottom of the potential (we set the Fermi energy $E_{\text{F}} = 0$). The cleaved-edge overgrown quantum wire corresponds to the case of a hard wall confinement. The corresponding confinement potential $V_{\text{conf}}(y)$ is sketched in figure 1(b). The effective potential, $V^{\sigma}_{\text{eff}}(y)$ within the framework of the Kohn–Sham density functional theory reads [8],

$$V^{\sigma}_{\text{eff}}(y) = V_{\text{H}}(y) + V^{\sigma}_{\text{xc}}(y), \tag{2}$$

where $V_{\text{H}}(y)$ is the Hartree potential due to the electron density $n(y) = \sum_{\sigma} n^{\sigma}(y)$ (including the mirror charges) [11],

$$V_{\text{H}}(y) = -\frac{e^2}{4\pi\varepsilon_0\varepsilon_r}\int_{-\infty}^{+\infty} \mathrm{d}y' n(y') \ln\frac{(y-y')^2}{(y-y')^2+4b^2}, \tag{3}$$

with b being the distance from the electron gas to the surface. The exchange and correlation potential $V_{\text{xc}}(y)$ in the local density approximation (LDA) is given by [8]

$$V^{\sigma}_{\text{xc}} = \frac{\delta}{\delta n^{\sigma}}\{n\epsilon_{\text{xc}}(n,\zeta)\} \tag{4}$$

where $\zeta = \frac{n^{\uparrow}-n^{\downarrow}}{n^{\uparrow}+n^{\downarrow}}$ is the local spin polarization. In the present paper we use a parametrization of the exchange and correlation energy ϵ_{xc} given by Tanatar and Ceperly (TC) [20]. Note that we also performed calculations on the basis of a parametrization recently provided by Attacalite *et al* [21] and found only a marginal difference with the results based on the TC functional.

The spin-resolved electron density in the wire can be expressed via the Green's function $G^{\sigma}(y, y, E)$ [22]

$$n^{\sigma}(y) = -\frac{1}{\pi}\,\text{Im}\left[\int_{-\infty}^{\infty} \mathrm{d}E\, G^{\sigma}(y,y,E) f_{\text{FD}}(E-E_{\text{F}})\right], \tag{5}$$

where $f_{\text{FD}}(E - E_{\text{F}})$ is the Fermi–Dirac distribution function. The Green's function, the Bloch states, the electron and current densities are calculated self-consistently using the technique described in detail in [11]. Knowledge of the wave vectors k^{σ}_{α} for different Bloch states α allows us to recover the subband structure, i.e. to calculate an overage position y^{σ}_{α} of the wavefunctions for different modes α for the given energy E [23],

$$y^{\sigma}_{\alpha} = \frac{\hbar k^{\sigma}_{\alpha}}{eB}. \tag{6}$$

We calculate the spin-resolved conductance of the wire on the basis of the linear response Landauer formula,

$$G^{\sigma} = \frac{e^2}{h}\sum_{\alpha}\int_{E^{\sigma}_{\text{th}\alpha}}^{\infty} \mathrm{d}E\left(-\frac{\partial f\,(E-E_{\text{F}})}{\partial E}\right), \tag{7}$$

where summation is performed over all propagating modes α for the spin σ, with $E^{\sigma}_{\text{th}\alpha}$ being the propagation threshold for αth mode. The current density for the mode α is calculated as [11]

$$J^{\sigma}_{\alpha}(y) = \frac{e^2}{h}V\int \mathrm{d}E\frac{j^{\sigma}_{\alpha}(y,E)}{v^{\sigma}_{\alpha}}\left(-\frac{\partial f\,(E-E_{\text{F}})}{\partial E}\right), \tag{8}$$

with v^{σ}_{α} and $j^{\sigma}_{\alpha}(y, E)$ being respectively the group velocity and the quantum mechanical particle current density for the state α at the energy E, and V being the applied voltage. All the calculations presented in this paper are performed for the temperature $T = 1$ K. In order to speed up the calculation we use the modified Broyden method [24] that allows one to reduce a number of iterations need to achieve a self-consistent solution from ∼2000 to only ∼50.

2.2. Split-gate quantum wires

We consider a split-gate quantum wire depicted in figure 1(a). To outline the role of the exchange and correlation interactions we first study the magnetotransport in the quantum wire within the Hartree approximation (i.e., when $V^{\sigma}_{\text{xc}}(y) = 0$, and the spin polarization is driven by Zeeman splitting of the energy levels). In our calculations we use parameters of the quantum wire indicated in figure 1. Figure 2(a) shows the one-dimensional (1D) electron density n^{σ}_{1D} for the spin-up and spin-down electrons in the quantum wire ($n^{\sigma}_{\text{1D}} = \int n^{\sigma}(y)\mathrm{d}y$). The distinguished feature of this dependence is a $1/B$-periodic, loop-like pattern of the density spin polarization $P_n = \frac{n^{\uparrow}_{\text{1D}}-n^{\downarrow}_{\text{1D}}}{n^{\uparrow}_{\text{1D}}+n^{\downarrow}_{\text{1D}}}$ as illustrated in figure 2(b). Figure 2(c) also shows the effective g factor. (We define the effective g factor according to $g^{\text{eff}} = \langle(E^{\uparrow}_{n,k} - E^{\downarrow}_{n,k})/g\mu_B B\rangle$ where the averaging is performed over the all k vectors and the occupied subbands n).

Figure 2(a) shows the number of spin-resolved subbands as a function of B. (Because the calculations are done for the finite temperature T, for a given magnetic field we count the subbands whose bottoms lie in the energy interval $E \lesssim E_{\text{F}} + 4kT$, where $4kT$ determines the energy window beyond which the Fermi–Dirac distribution rapidly decays to zero). The pronounced feature of this dependence is that the number of subbands is always even, $N = 2, 4, 6, \ldots$, such that the spin-up and spin-down subbands depopulate simultaneously. The spin polarization is apparently directly related to the magnetosubband structure: the polarization drops almost to zero at the magnetic fields when the subbands depopulate. In order to understand the origin of the spin polarization let us analyze the evolution of the subband structure as the applied magnetic field varies. Let us concentrate on the polarization loops in the field interval $1.3\ \text{T} \lesssim B \lesssim 2.6\ \text{T}$ when the number of the spin-resolved subbands $N = 4$ and the filling factor in the middle of the wire $2 \leqslant \nu(0) \leqslant 4$.

Figure 3(a) shows the filling factor $\nu^{\sigma}(y)$, current densities $J^{\sigma}_{\alpha}(n)$, and the magnetosubband structure for the magnetic field $B = 1.35$ T. This field corresponds to the case when the fifth and sixth spin-resolved subbands just became depopulated, i.e. their bottoms are situated at $\gtrsim E_{\text{F}} + 4kT$. The bottoms of third and fourth subbands are situated below the Fermi energy and are fully populated. As a result, the electron density is constant, which corresponds to a formation of the incompressible strip. Because of the spin-up and spin-down subbands are fully filled, the corresponding electron densities are equal and the spin polarization of the electron density is zero. When magnetic field is raised the subbands are pushed up in the energy and the two highest spin-resolved subbands, following Chklovslii *et al* scenario [6], become pinned at the Fermi energy. The subband bottoms flatten which

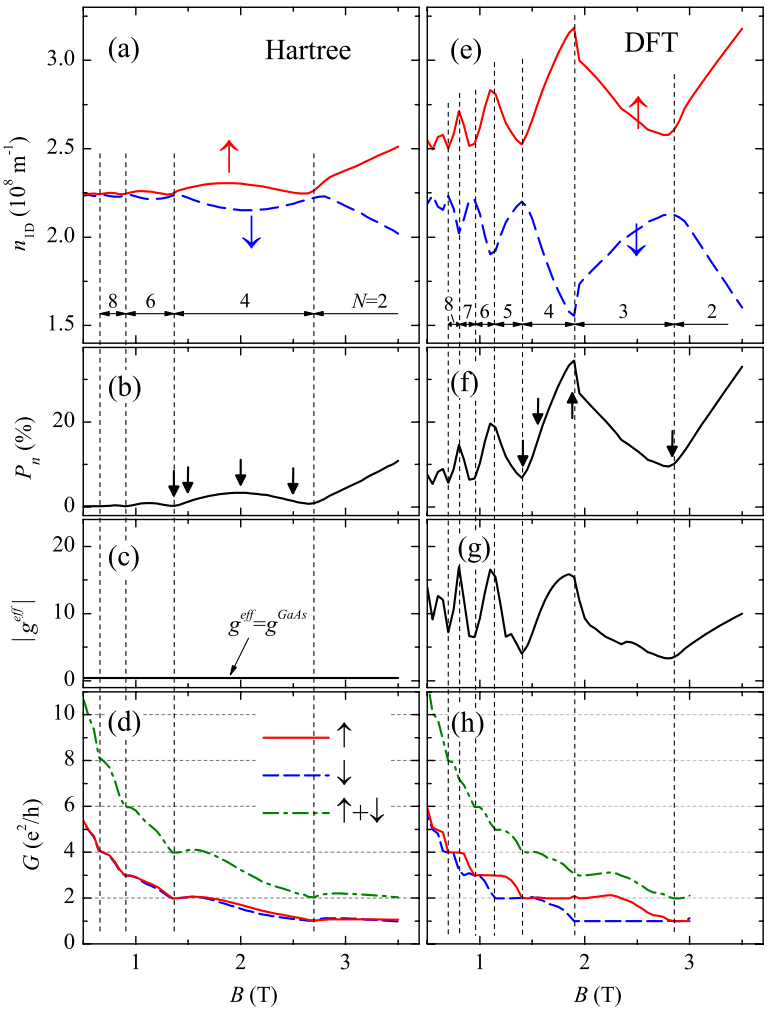

Figure 2. (a), (e) One-dimensional charge density for the spin-up and spin-down electrons, $n_{1D}^{\uparrow}$, $n_{1D}^{\downarrow}$ and the number of occupied subbands N; (b), (f) spin polarization of the charge density, $P_n = \frac{n_{1D}^{\uparrow} - n_{1D}^{\downarrow}}{n_{1D}^{\uparrow} + n_{1D}^{\downarrow}}$; (c), (g) the effective g factor, and (d), (h) the total and the spin-resolved conductances. Parameters of the quantum wire are indicated in figure 1. Left and right panels correspond to the Hartree and DFT calculations. The magnetosubband structure for the magnetic fields indicated by arrows in (b), (f) is shown in figure 3. (Figure is adapted from [11, 19].)

signals the formation of the compressible strip in the middle of the wire, see figure 3(b). When the subband bottoms reach the energy $E \approx E_F - 4kT$, the subbands become partially occupied. The partial subband occupation combined with their energy separation due to the Zeeman interaction results in a different population for the spin-up and spin-down electrons. With increase of the magnetic field the filling factor decreases, but the spin polarization increases until the subband bottoms approach $\sim E_F$, figure 3 (c). This magnetic field corresponds to the maximal spin polarization $P_n \sim 3\%$. With further increase of the magnetic field, the subbands bottoms are pushed up above E_F, which causes further decrease of the filling factor and diminishing screening efficiency. As the result, the width of the compressible strip decreases until the upper subbands become completely depopulated and the incompressible strip forms again in the middle of the wire, see figure 3(d). This is accompanied by a gradual decrease of the density polarization P_n to zero.

The described above picture of evolution of the density polarization qualitatively holds for all other polarization loops. When magnetic field exceeds $B = 2.6$ T, only two subbands survive in the quantum wire. With further increase of magnetic field the upper (spin-up) subband gradually depopulates and the density polarization P_n grows linearly until it reaches 100% when only the spin-down subband remains in the wire.

As we mentioned before, the Hartree approximation predicts that spin-up and spin-down subbands depopulate simultaneously and thus the conductance drops in steps of $2e^2/h$ as the magnetic field increases (figure 2(d)). This is in strong disagreement with the experimental observations that demonstrate that the subbands depopulate one by one such that the conductance decreases in steps of e^2/h. We will show below that accounting for the exchange and correlation interactions leads to qualitatively new features in the subband structure and brings the theory to a close agreement with the experiment.

Figures 2(e)–(h) and 3(e)–(h) shows the electron density, conductance and subband structure for the quantum wire calculated using the DFT within LDA. The main differences in comparison to the case of spinless electrons (Hartree

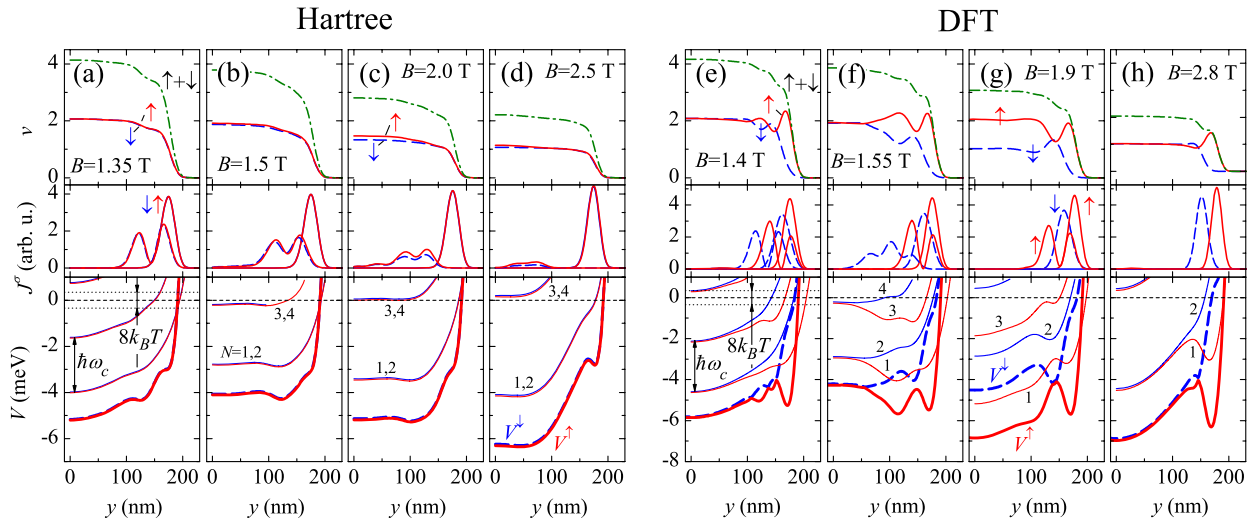

Figure 3. Upper panels: the local filling factor $\nu(y) = n(y)/n_B$, $(n_B = eB/h)$ for spin-up and spin-down electrons calculated in the Hartree and DFT approximations for several representative magnetic fields (shown by arrows in figures 2(b) and (f)). Middle panels: the current density distribution (in arbitrary units) for spin-up and spin-down electrons calculated according to equation (8). Lower panels: magnetosubband structure for spin-up and spin-down electrons (solid and dashed lines correspondingly). Fat solid and dashed lines indicate the total confining potential $V^\sigma(y)$ (equation (1)). The subband numbers N are indicated in the lower panel. (Figure is adapted from [11].)

approximation) can be summarized as follows. First, the spin polarization P_n and the effective g factor show a pronounced $1/B$-periodic loop-like pattern which is an order of magnitude higher in comparison to the Hartree approximation. Second, the magnetosubbands depopulate one by one, and the conductance decreases in steps of e^2/h. Third, the outermost edge states become spatially polarized (separated), which is in the strong contrast with the Hartree approximation, where they are situated practically at the same distance from the wire boundary.

In order to understand the effect of the exchange–correlation interactions on the energetics and the magnetosubband structure of the quantum wire, let us concentrate on the same field interval as discussed in the case of the Hartree approximation. A comparison between figures 3(a)–(d) and (e)–(h) demonstrates that evolution of the magnetosubband structure calculated within the DFT approximation follows the same general pattern as for the case of the Hartree approximation. In particular, a depopulation of the subbands starts from the wire edges and the subbands remain pinned in the central region of the wire until they are eventually pushed up by magnetic field. The major difference from the Hartree case is that Hartree subbands are practically degenerated and depopulate together, whereas this degeneracy is lifted by the exchange interaction such that the DFT subbands depopulate one by one. This is because that in the compressible region the subbands are only partially filled (because $f_{\rm FD} < 1$ in the window $|E - E_{\rm F}| \lesssim 2\pi kT$), and, therefore, the population of the spin-up and spin-down subbands can be different (and can be easily changed). In the DFT calculation, this population difference (triggered by Zeeman splitting) is strongly enhanced by the exchange interaction leading to different effective potentials for spin-up and spin-down electrons and eventually to the subband spin splitting with the magnitude that can be comparable to the Landau level spacing $\hbar\omega_c$.

Let us now discuss the effect of the exchange interaction on the structure of the edge states. At sufficiently high magnetic field and for sufficiently smooth confining potentials the compressible and incompressible strips start to form near the wire boundaries. A quantitative analytical description of the edge states in terms of the compressible and incompressible strips was first given in the seminal papers of Chklovskii *et al* [6], and a corresponding theory has been the basis for understanding of various features of the magnetotransport phenomena in the quantum Hall regime.

In order to outline the effect of the exchange interaction on the structure of the compressible strips we first perform calculations in the Hartree approximation (setting $V^\sigma_{\rm xc}(y) = 0$) and, following Suzuki and Ando [25] compare them to the predictions of Chklovskii *et al* [6]. According to the Chklovskii *et al* theory [6] the width and position of the compressible and incompressible strips are determined by the filling factor $\nu(0)$ in the bulk (i.e. in the middle of the wire, $y = 0$), and the depletion length l. Figure 4 shows the electron density profiles (the local filling factors) $\nu(y) = n(y)/n_B (n_B = eB/h)$ and magnetosubband structures for two representative values of the depletion lengths l illustrating a formation of the compressible strips near the wire edges. (Following Suzuki and Ando [25] we define the width of the compressible strip $w^H_{\rm comp}$ within the energy window $|E - E_{\rm F}| < 2\pi kT$; the depletion length l is extracted from the calculated self-consistent density distribution by fitting to the Chklovskii *et al* dependence [6] $n(y) = n(0)(\frac{y-l}{y+l})^{1/2}$.) Our calculations reconfirm a good agreement between the Chklovskii *et al* electrostatic theory and the Hartree approximation demonstrated earlier by Suzuki and Ando [25].

Let us now turn to the effect of the exchange interaction on the structure of the compressible strips. Figure 4(a) shows the electron density profiles $\nu(y) = n(y)/n_B$ calculated in

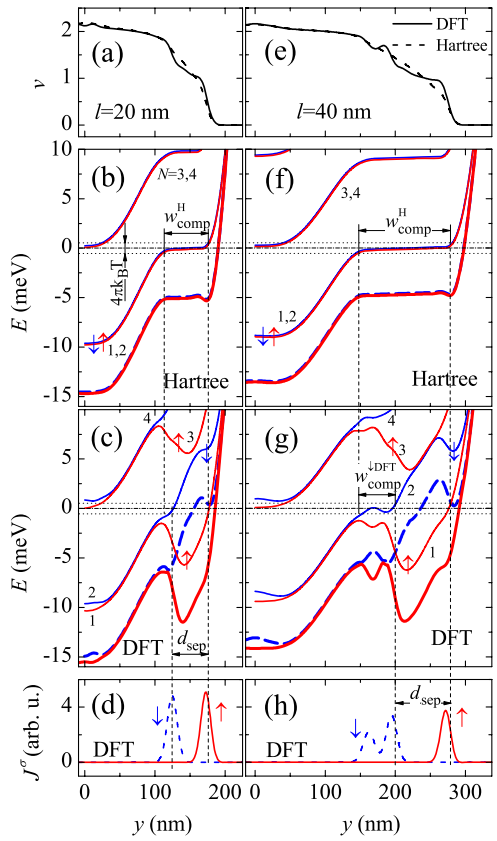

Figure 4. (a), (e) The electron density profile (the local filling factor) $\nu(y) = n(y)/n_B$; (b), (c), (f), (g) the magnetosubband structure and (b), (f) the current density distribution (in arbitrary units) in wires the depletion lengths $l = 20$ and 40 nm (left and right columns respectively) calculated in the Hartree and the DFT approximations. Fat solid and dashed lines show the total confining potentials for spin-up and spin-down electrons (equation (1)). The subband numbers N are indicated in the lower panel. Parameters of the wires: $V_0 = -0.2$ eV; $\hbar\omega_0 = 3$ meV, 1 meV (first and second columns respectively). The corresponding magnetic fields are $B \approx 5.9$ T, 4.9 T; and the electron density $n(0) \approx (3, 2.5) \times 10^{15}$ m^{-2}. $T = 1$ K, $E_F = 0$. (Figure is adapted from [12].)

the Hartree and DFT approaches for a representative filling factor $\nu(0) \approx 2.2$. As expected, the density profiles are very similar, whereas the corresponding subband structures are strikingly different. In the Hartree approximation the spin degenerate $N = 1, 2$ subbands form a compressible strip of the width $w^H_{\rm comp}$, see figure 4(b). Figures 4(c) and (g) show corresponding subband structure in the DFT approximation, where exchange interaction lifts the spin degeneracy by pushing the spin-up and spin-down subbands respectively below and above the Fermi energy. As a result, the compressible region (present in the Hartree approximation) is suppressed and the spin-up and spin-down states become spatially separated by the distance $d_{\rm sep} \approx w^H_{\rm comp}$. This is illustrated in figures 4(d), (h) which show the current densities for the outermost spin-up and spin-down channels, peaked at the positions where the corresponding spin-up and spin-down subbands intersect the Fermi energy. (The current densities in the Hartree approximation are practically degenerate and delocalized within the whole extension of the compressible strip.)

The scenario of the suppression of the compressible strips described above holds also for larger l and B, with one new important feature. According to electrostatic description of Chklovskii *et al* [6], the compressible strips are more easily formed in a structure with larger depletion length l (i.e. with more smooth confinement), which is confirmed experimentally [26]. This feature is clearly manifest in the Hartree calculations, figures 4(b) and (f), where the width of the compressible strip grows as l is increased. When l is small as in figure 4(c), the exchange interaction completely suppresses the compressible strip and the spin-up and spin-down spin channels becomes spatially separated with $d_{\rm sep} \approx w^H_{\rm comp}$ as described above. For larger l the compressible strip of the width $w^{\downarrow\rm DFT}_{\rm comp}$ starts to form for the spin-down subband (figure 4(f)), such that $d_{\rm sep} + w^{\downarrow\rm DFT}_{\rm comp} \approx w^H_{\rm comp}$, see figure 4(f). With further increase of the depletion length l the compressible strip of the width $w^{\uparrow\rm DFT}_{\rm comp}$ starts to form also for the spin-up edge channels.

The above analysis demonstrates that the exchange interaction suppresses formation of the compressible strips and leads to a spatial separation between the spin-up and spin-down states. This conclusion, outlining the importance of the exchange interaction, represents a significant departure from the conventional spinless Chklovskii *et al* picture of edge states [6] widely used for analysis of magnetotransport experiments in the edge state regime. It should be noted that the exchange interaction in a qualitatively similar way affects the edge states around quantum antidots leading to the spatial separation between the spin-up and spin-down states [14]. There are however, important differences between the structure of the edge states in the quantum wires and the antidots. This difference is due to an enhanced screening in the antidot structures, which is discussed in detail in [14].

Finally, it is worth mentioning that we have recently performed a detailed comparison of the self-consistent calculations based on the Hartree–Fock and the spin density functional theory for a split-gate quantum wire in the integer quantum Hall regime [19]. We demonstrated that these approaches provide qualitatively (and in most cases quantitatively) same description of a split-gate quantum wire. This includes the electron density, spin polarization and the effective g factor. Both approaches give the same values of the magnetic fields corresponding to the successive subband depopulation and qualitatively similar evolution of the magnetosubbands. Quantitatively, however, the HF and the DFT subbands are different (even though the corresponding total electron densities are practically the same). In contrast to the HF approach, the DFT calculations predict much larger spatial spin separation near the wire edge for the low fields (when the compressible strips for spinless electrons are not formed yet).

2.3. Cleaved-edge overgrown quantum wires

Recent advances in fabrication of low dimensional structures allow one to create quantum wires with a hard wall potential confinement. One of the most widely used techniques for fabrication of quantum wires with such the confinement is the

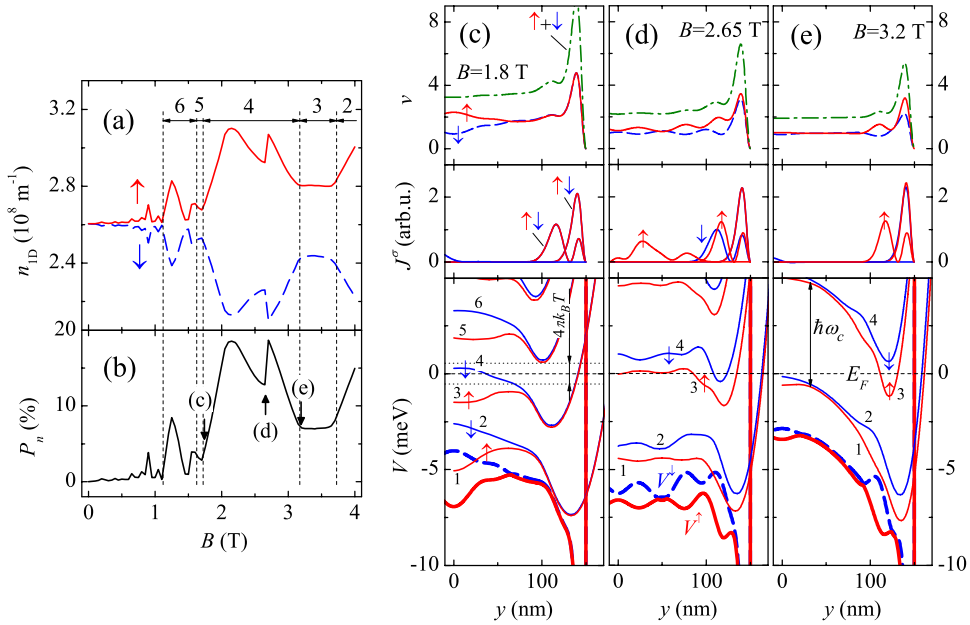

Figure 5. (a) One-dimensional charge density for the spin-up and spin-down electrons, $n_{1D}^{\uparrow}$, $n_{1D}^{\downarrow}$, and the number of occupied subbands N in a cleaved-edge overgrown quantum wire calculated in the DFT approximation; (b) the spin polarization of the charge density, $P_n = \frac{n_{1D}^{\uparrow} - n_{1D}^{\downarrow}}{n_{1D}^{\uparrow} + n_{1D}^{\downarrow}}$. Arrows in (b) indicate the magnetic field corresponding to the magnetosubband structure shown in figures (c) and (d). (c), (d) The subband structure for magnetic fields indicated by arrows in (b). Upper panels: electron density profiles (local filling factors) $\nu(y) = n(y)/n_B$ for spin-up and spin-down electrons; middle panels: the current density distribution for spin-up and spin-down electrons; lower panels: magnetosubband structure for spin-up and spin-down electrons. Fat solid and dashed lines indicate the total confining potential for respectively spin-up and spin-down electrons (equation (1)). The parameters of the wire are indicated in figure 1. (Figure is adapted from [13].)

molecular beam epitaxy double-growth technique [27]. The technique of the cleaved-edge overgrowth was extensively used to design samples with a tunnel probe in direct contact with the edge of a two-dimensional electron system (2DES) (for a review see e.g. [28]).

Recent experiments indicate that the standard description of the edge states developed for the quantum wires with a smooth confinement based on the concept of compressible and incompressible strips does not apply to the case of a sharp-edged 2DEG [29]. At the same time a rigorous theory for the edge state structure in hard wall quantum wires accounting for electron–electron interaction and spin effects has not been reported until recently. In this section we provide a brief account of the structure of the edge states and magnetosubband evolution in hard wall quantum wires in the integer quantum Hall regime calculated on the basis of the self-consistent Green's function technique where the electron interaction and spin effects are included within the density functional theory in the local spin density approximation [13].

We consider a quantum wire which is infinitely long in the x-direction and is confined by a hard wall potential in the y-direction, see figure 1(b). The Hamiltonian and details of calculation are described in section 2.1. Figure 5 shows the electron density and density spin polarization P_n as a function of magnetic field as well as evolution of the magnetosubband structure calculated within the spin-DFT approach. There is a certain similarity in the behavior of P_n as well as in overall evolution of the magnetosubband structure in comparison to the case of a split-gate quantum wire. However, in contrast to the wires with a smooth confinement, the spin polarization of the electron density in the cleaved-edge overgrown wires shows a pronounced double-loop pattern (in contrast to the single loop pattern in the wires with a smooth confinement, cf figure 2(b)). The magnetosubband structure and the density distribution in the hard wall quantum wire is qualitatively different from that one with a smooth electrostatic confinement. In particular, in the hard wall wire a deep triangular potential well of the width $\sim l_B$ (with l_B being the magnetic length) is formed in the vicinity of the wire boundary. The wavefunctions are strongly localized in this well which leads to the increase of the electron density near the edges.

Because of a presence of the deep triangular well near the wire boundaries, the subbands start to depopulate from the central region of the wire and remain pinned in the well region until they are eventually pushed up by an increasing magnetic field. This is illustrated in figures 5(c)–(e) showing depopulations of subbands $N = 2, 3$. This character of the subband depopulation is different from the case of a smooth confinement where depopulation of the subbands starts from the edges and extends towards the wire center as the magnetic field increases. A pronounced double-loop pattern of P_n can be traced to the successive depopulation of the magnetosubbands, where the second loop feature is related to the presence of the well near the edge.

Finally, in contrast to the case of a smooth confinement, in the hard wall wires the compressible strips do not form in the vicinity of wire boundaries and a spatial spin separation between spin-up and spin-down states near the edges is absent.

3. Conductance of quantum point contacts and open dots

3.1. Model and method

We consider an open structure (e.g. a quantum point contact (QPC) or a quantum dot) placed between two semi-infinite electron reservoirs [16–18]. A schematic layout of the device is illustrated in figure 6. Charge carriers originating from a fully ionized donor layer form the two-dimensional electron gas (2DEG) which is buried inside a substrate at the GaAs/$Al_xGa_{1-x}As$ heterointerface at the distance b from the surface. Metallic gates are situated on the top of the heterostructure and define a central (device) region as well as electron reservoirs that are represented by uniform quantum wires of the infinite length.

The Hamiltonian of the whole system (the internal region + the semi-infinite leads) within the Kohn–Sham formalism can be written in the form $H = \sum_\sigma H^\sigma$, [16–18]

$$H^\sigma = -\frac{\hbar^2}{2m^*}\nabla^2 + V^\sigma(\mathbf{r}), \tag{9}$$

$\mathbf{r} = (x, y)$, $m^* = 0.067m_e$ is the GaAs effective mass and σ stands for spin-up, $\uparrow$, and spin-down, $\downarrow$, electrons. The first term in (1) is the kinetic energy of an electron while $V^\sigma(\mathbf{r}) = V_{\rm conf}(\mathbf{r}) + V_{\rm H}(\mathbf{r}) + V^\sigma_{\rm xc}(\mathbf{r})$ is the total confining potential which is a sum of the electrostatic confinement potential, the Hartree potential, and the exchange–correlation potential, respectively. The electrostatic confinement $V_{\rm conf}(\mathbf{r}) = V_{\rm gates}(\mathbf{r}) + V_{\rm donors} + V_{\rm Schottky}$ includes contributions from the top gates, the donor layer and the Schottky barrier. The explicit expressions for the potentials $V_{\rm gates}(\mathbf{r})$ and $V_{\rm donors}$ are given in [9, 10]; the Schottky barrier is chosen to be $V_{\rm Schottky} = 0.8$ eV. The Hartree potential is written in a standard form [8]

$$V_{\rm H}(\mathbf{r}) = \frac{e^2}{4\pi\varepsilon_0\varepsilon_r}\int {\rm d}\mathbf{r}'n(\mathbf{r}')\left(\frac{1}{|\mathbf{r}-\mathbf{r}'|} - \frac{1}{\sqrt{|\mathbf{r}-\mathbf{r}'|^2+4b^2}}\right),$$

where $n(\mathbf{r}) = \sum_\sigma n^\sigma(\mathbf{r})$ is the total electron density and the second term describes the mirror charges placed at the distance b from the surface, $\varepsilon_r = 12.9$ is the dielectric constant of GaAs, and the integration is performed over the whole device area including the semi-infinite leads.

The exchange–correlation potential $V^\sigma_{\rm xc}(\mathbf{r})$ in the local spin density approximation is given by the functional derivative [8] equation (4). For the exchange and correlation energy functional $\epsilon_{\rm xc}$ we have employed two commonly used parameterizations, by Tanatar and Ceperley [20] and by Attacalite *et al* [21]. These two parameterizations give very similar results. All the results presented below correspond to the parametrization of Tanatar and Ceperley [20].

The central quantity in transport calculations is the conductance. In the linear response regime, it is given by the Landauer formula $G = \sum_\sigma G^\sigma$, [22]

$$G^\sigma = -\frac{e^2}{h}\int {\rm d}E\; T^\sigma(E)\frac{\partial f\,(E-E_{\rm F})}{\partial E}, \tag{10}$$

where $T^\sigma(E)$ is the total transmission coefficient for the spin channel σ, $f(E-E_{\rm F})$ is the Fermi–Dirac distribution function

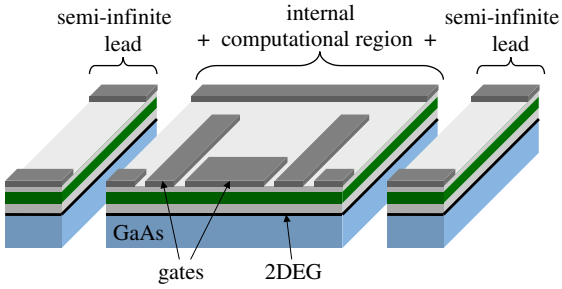

Figure 6. Schematic geometry of an open structure. The internal region is attached to two semi-infinite quantum wires which serve as the electron reservoirs. Metallic gates on the top of the structure defines electrostatic confinement.

and $E_{\rm F}$ is the Fermi energy. The main steps of calculations of $T^\sigma(E)$ are briefly presented below (see [16, 17] for details).

We discretize equation (1) and introduce the tight-binding Hamiltonian where the lattice constant is chosen to be sufficiently small to ensure that the tight-binding Hamiltonian is equivalent to the continuous Schrödinger equation. The retarded Green's function is introduced in a standard way [22],

$$\mathcal{G}^\sigma = (E - H^\sigma + {\rm i}\eta)^{-1}. \tag{11}$$

The Green's function in the real space representation, $\mathcal{G}^\sigma(\mathbf{r}, \mathbf{r}, E)$, provides an information about the electron density at the site $\mathbf{r}$, [22]

$$n^\sigma(\mathbf{r}) = -\frac{1}{\pi}\,{\rm Im}\int {\rm d}E\,\mathcal{G}^\sigma(\mathbf{r},\mathbf{r},E)\,f(E-E_{\rm F}). \tag{12}$$

Note that $\mathcal{G}^\sigma(\mathbf{r}, \mathbf{r}, E)$ is a rapidly varying function of energy. As a result, a direct integration along the real axis in equation (12) is rather ineffective as its numerical accuracy is not sufficient to achieve a convergence of the self-consistent electron density. Because of this, we transform the integration contour into the complex plane ${\rm Im}[E] > 0$, where the Green's function is much more smoother (see [16] for details).

In order to calculate the Green's function of the whole system we divide it into three parts, an internal region and two semi-infinite leads, as shown in figure 6. The internal region consists of the device region as well as a part of the leads. In order to link the internal region and the leads together the self-consistent charge density (and the potential) at both sides must be the same. To fulfill this requirement, we place the semi-infinite leads far away from the central region so that the gates defining the device do not affect the electron density distribution in the leads. As a result, it is fully justified to approximate the semi-infinite leads by an uniform quantum wire. The self-consistent solution for the latter can be found by the technique developed in [11] and described in section 2.1. Eventually, the Green's function of the whole system is calculated by linking the surface Green's function for the semi-infinite leads (calculated using the technique of [11]) and the Green's function of the internal region with the help of the Dyson equation [30].

All the calculations described above are performed self-consistently in an iterative way until a converged solution for

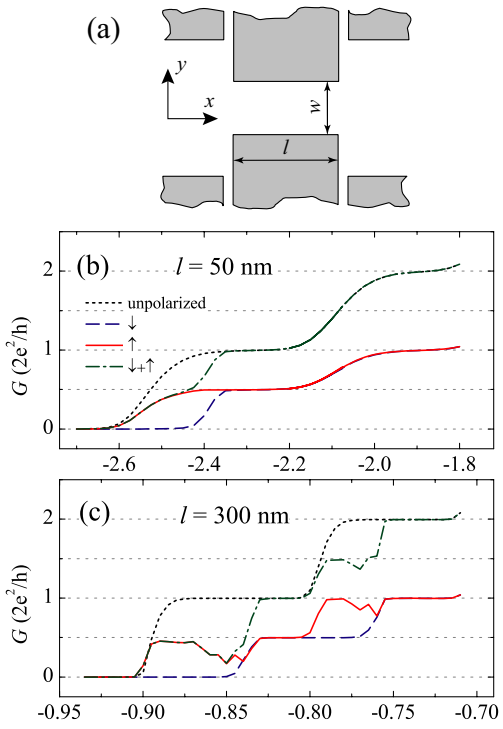

Figure 7. (a) Schematic geometry of the gates that form a constriction of length l and width w; conductance of the quantum point contact of the length (b) $l = 50$ nm and (c) $l = 300$ nm as a function of the gate voltage V_g. The geometrical width of the constriction is $w = 100$ nm. The dashed line corresponds to the spin-unpolarized solution. Parameters of the QPC are as follows: The 2DEG is buried at $b = 70$ nm below the surface (the widths of the cap, donor and spacer layers are 24, 36 and 10 nm respectively), the donor concentration is 0.6×10^{24} m^{-3}. The width of the semi-infinite leads is $w_{\text{lead}} = 400$ nm, $T = 0.2$ K. (Figure is adapted from [17].)

the electron density and potential (and hence for the total Green's function) is obtained. Having calculated the total self-consistent Green's function, the scattering problem is solved using the standard Green's function technique in magnetic field [30].

The self-consistent solution in quantum transport or electronic structure calculations is often found using a 'simple mixing' method. It is the most robust and reliable algorithm with only one disadvantage, namely a low convergence rate. The charge density on the $(i+1)$-th iteration loop is updated through the input $n_i^{\text{in}}(\mathbf{r})$ and output $n_i^{\text{out}}(\mathbf{r})$ densities on the previous ith iteration

$$n_{i+1}^{\text{in}}(\mathbf{r}) = (1-\epsilon)n_i^{\text{in}}(\mathbf{r}) + \epsilon n_i^{\text{out}}(\mathbf{r}), \tag{13}$$

with ϵ being a small constant ~0.1–0.01. It is typically needed ~200–2000 iteration steps to achieve our convergence criterion for the relative density update on the ith iteration step,

$$\frac{|n_i^{\text{out}} - n_i^{\text{in}}|}{n_i^{\text{out}} + n_i^{\text{in}}} < 10^{-7}, \tag{14}$$

where $n = \int n(\mathbf{r})\,\mathrm{d}\mathbf{r}$ is the total electron number in the internal region during the ith iteration step.

The self-consistent calculation are performed for different gate voltages. To facilitate the calculations we use a solution from the previous value of the gate voltage as an initial guess for the subsequent one. It is worth noting that the modified Broyden's second method [24], which can greatly reduce a number of iterations for the case of spinless electrons, does not always lead to reliable convergent results in the presence of the spin degree of freedom (i.e. for the case of the QPC addressed in section 3.2).

Finally, a comment is in order concerning an applicability of the developed method. The conductance calculations in open structures presented in this paper are based on an approach that during recent years became a standard tool for transport *ab initio* calculations in molecular junctions, atomic wires and related systems [31–37]. Its starting point is the Landauer-type formula where the conductance is calculated using the nonequilibrium Green function technique (NGFT) or similar methods combined with the density functional theory in the local density approximation. The formal justification of this approach is given in [34, 38–40]. This approach has witnessed a great success in reproducing observed I–V characteristics of molecular and metallic junctions, notably in the strong coupling limit (when the conductance exceeds the conductance unit $G_0 = 2e^2/h$). At the same time, for weakly coupled systems such as organic molecules the standard NGFT + DFT approach leads to the orders-of-magnitude discrepancy between the measured and calculated currents and to incorrect predictions of the conducting (instead of experimentally observed insulating) phase [34–37]. It has been recently recognized that the failure of this approach in the weak coupling regime can be traced to spurious self-interaction errors caused by the lack of the derivative discontinuity of the exchange and correlation potential in the standard DFT [5, 34–37]. It has been demonstrated recently that elimination of the self-interactions errors and restoring agreement with the experiment for the case of the weak coupling requires approaches and the exchange and correlation functionals that go beyond the standard NGFT + DFT scheme [34–37]. Because of this our present mean-field approach is not expected to work for the case of the weak coupling (i.e. in the Coulomb blockade regime when the conductance of each QPC connecting the dot to the reservoirs is reduced below the conductance unit G_0), and its applicability is limited to the case of open structures when the electron number in the device is not quantized and the Coulomb charging is unimportant.

3.2. Quantum point contact

In this section we discuss a conductance of split-gate QPCs with parameters representative for a typical experimental structure, see figure 7(a). Figures 7(b) and (c) show the conductance of the QPCs with the constriction lengths $l = 50$ nm (a very short QPC) and $l = 300$ nm (a long quantum wire-type QPC) [17]. The conductance of the QPCs shows a broad plateau-like feature at $0.5 \times 2e^2/h$. As the length of the constriction increases, a dip following the 0.5-plateau starts to develop in the QPC conductance. An inspection of

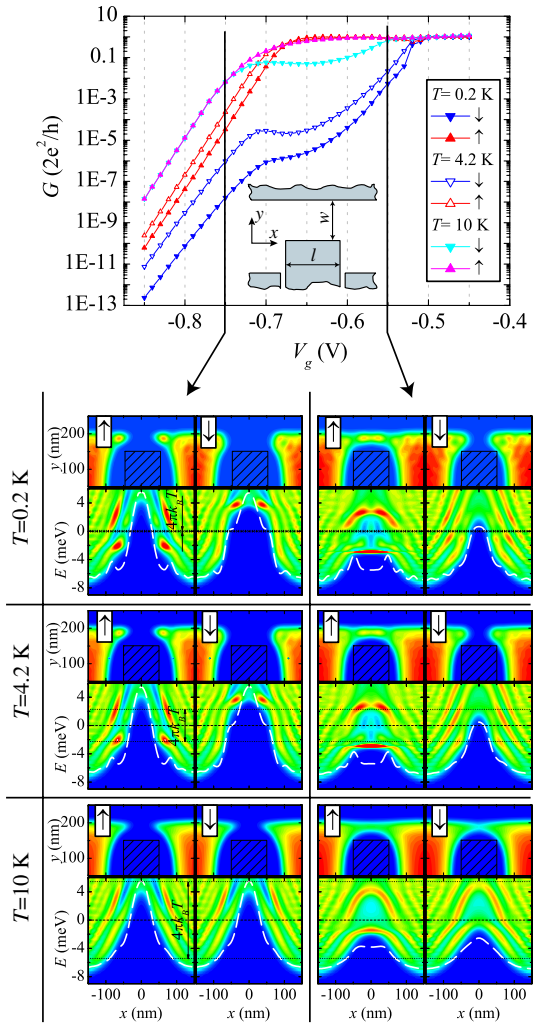

Figure 8. Evolution of quasi-bound states in the quantum point contact for different temperatures and gate voltages. The charge density and the local density of states in the QPC at the gate voltages as indicated in the conductance plot in the inset (note the log scale of the conductance). Parameters of the QPC are as follows: The length of the constriction is $l = 100$ nm, the width of the constriction is $w = 100$ nm, the 2DEG is buried at $b = 70$ nm below the surface (the widths of the cap, donor and spacer layers are 24, 36 and 10 nm respectively), the donor concentration is 0.6×10^{24} m^{-3}. The width of the semi-infinite leads is $w_{\rm lead} = 500$ nm, $T = 0.2$, 4.2 and 10 K.

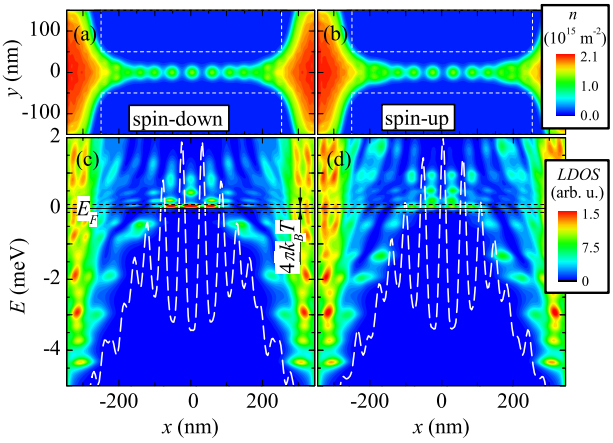

Figure 9. Formation of the quasi-bound states in a long QPC. The top panel shows the electron densities in the QPC revealing a formation of spin-polarized charge droplets resembling the spin density waves. The bottom panel shows the local density of states. The white dashed lines indicate the total effective potential along the QPC. Parameters of the QPC are as follows: the length of the constriction is $l = 500$ nm, the width of the constriction is $w = 100$ nm, the 2DEG is buried at $b = 70$ nm below the surface (the widths of the cap, donor and spacer layers are 24, 36 and 10 nm respectively), the donor concentration is 0.6×10^{24} m^{-3}. The width of the semi-infinite leads is $w_{\rm lead} = 400$ nm, $T = 0.2$ K.

the spin-resolved conductance demonstrates that the 0.5 feature corresponds to the transmission of only one spin channel (say, spin-up), whereas the second (spin-down) conductance channel is totally suppressed. For long constrictions ($l \gtrsim 300$ nm) the 0.5 plateau starts to 'wear down' transforming into a broad feature whose maximal amplitude is less than $0.5 \times 2e^2/h$. If the constriction is sufficiently long ($l \gtrsim 100$ nm), a conductance plateau at $\sim 1.5 \times 2e^2/h$ starts to develop and a conductance dip following the 1.5-plateau also starts to emerge as the length of the constriction increases. We stress that these results are generic; we studied QPCs with lengths in the range 40–500 nm and electron densities in the leads in the range 10^{15}–4×10^{15} m^{-2}, with very similar results [17].

To shed light on a microscopic origin of the $0.5 \times 2e^2/h$ conductance feature and the suppression of the spin-down channel let us inspect the charge density and the local density of states (LDOS) of the QPC. Figure 8 shows the charge densities and the LDOS in the QPC close to the pinch-off regime and for the case of one transmitted spin-up, $G^{\uparrow} = e^2/h$, and a totally blocked spin-down, $G^{\downarrow} = 0$, channel. Already in the pinch-off regime, two spin-polarized quasi-bound states are developed at both sides of the constriction. The quasi-bound states are not spatially fixed but gradually move towards each other and eventually merge during the sweep of the gate voltage $V_{\rm g}$. Our conclusions concerning the spin polarization in the constriction are consistent with earlier findings based on the spin-DFT calculations [41–45]. The features of the evolution and formation of the localized spin-polarized quasi-bound states in the QPC agree well with the results reported by Hirose *et al* [45] and Rejec and Meir [46]. The spin polarization is caused by the exchange interaction which dominates the kinetic energy for low densities. The quasi-bound states for corresponding droplets can also be traced in the LDOS, see figure 8. It is interesting to note that the spin polarization survives up to temperatures ~6–8 K and becomes quenched around $T \sim 10$ K. The spin polarization leads to the spatial separation between spin-up and spin-down states. This is reflected in the shape of the total confining potential for the spin-down electrons that forms a wide tunneling barrier, see figure 8. Because of this barrier, the transmission probability for the spin-down conductance is negligibly small, whereas the second (spin-up) channel can be completely transmitted leading to the conductance $G \approx 0.5 \times 2e^2/h$. In the case of a long, quantum wire-type constriction, the electron density show a signature of formation of the spin density waves, with spatially separated spin-up and spin-down quasi-bound states, see figure 9.

Let us now compare the spin-DFT-based conductance calculations reported above with the experimental conductance of the QPC structures. The common feature of the calculated conductance is the pronounced plateau-like feature at $\sim 0.5 \times 2e^2/h$ for all QPC structures studied (both short and long ones). For longer QPCs ($l \gtrsim 150$ nm), a dip following 0.5-plateau starts to develop in the conductance. On the contrary, the experimental data clearly show an anomaly in the conductance around $0.7 \times 2e^2/h$ [47–50]. (It should be stressed that the calculated 0.5 plateau corresponds to the complete suppression of one spin channel, whereas experimentally observed 0.7-anomaly means that both spin channels have to be present in the conductance [50].) *The above comparison demonstrates that while the spin-DFT-based 'first-principle' calculations predict the spin polarization in the QPC structure, the calculated conductance clearly does not reproduce the 0.7-anomaly observed in almost all QPCs of various geometries.*

In order to understand why the calculated conductance fails to reproduce the 0.7-anomaly, let us critically analyze the major features of the DFT-based conductance calculations. We focus below on several aspects of the DFT approach that seem to be the most important for understanding of the discrepancy between the calculations and the experiment.

The question concerning the validity of the DFT approach relies on a proper description of the exchange and correlation within the DFT approximation. The exchange and correlations are commonly accounted for within the local spin density approximation [8] using two popular parameterizations, namely the parametrization of Tanatar and Ceperley [20] and Attacalite *et al* [21]. The validity of these approximations has been tested for few-electron quantum dot systems and, generally, a very good agreement with the exact diagonalization and/or variational Monte Carlo calculations was found [51]. Taking into account that these parameterizations give practically the same results for the QPC conductance, we do not expect the utilization of the above parameterizations to be a source of a significant discrepancy between the calculated conductance and the experiment. Instead, we focus on another aspect of the choice of the exchange energy functional which arises in the systems with a variable particle number. (Note that the QPC structure, being an essentially open structure, belongs to this class of systems.) As we mention in the previous section, the developed method is not expected to work for the systems when transport is mediated by weakly coupled quasi-bound states. This aspect is related to the infamous 'derivative discontinuity problem' of the DFT originating from the discontinuous dependence of $V_{\rm xc}$ on the particle number [8]. (Note that the LDA does not include any derivative discontinuity in the $V_{\rm xc}$.) Several recent studies have identified the lack of the derivative discontinuity in LDA as a major source of error in the DFT-based transport calculations [35, 36] in atomic systems. For example, Toher *et al* [35] argued that LDA approximation is not suitable for transport calculations for the case of weak coupling. Note that various approaches to the description of quantum transport for the case of weakly coupled systems (accounting for the charge quantization and thus eliminating the self-interaction errors) were discussed in [34] and [37].

We argue here that a similar problem related to the derivative discontinuity may be the reason why the standard DFT + LDA approach fails to describe the observed 0.7-anomaly in the QPC. Indeed, the formation of the spin-polarized charge droplet predicted by the DFT + LDA approach implies that electrons are trapped in weakly coupled quasi-bound states in the center of the QPC. As mentioned above, in the case of weak coupling the lack of the derivative discontinuity in the LDA approximation causes the orders-of-magnitude discrepancies between the theory and experiment for the molecular systems. Thus, one can expect that due to the same reason the LDA approximation is not suitable for the case of the QPC structure as well. Because the corrective schemes accounting for the derivative discontinuity are shown to strongly affect the electron density and the energy levels in the system [35], and because of the apparent failure of the standard DFT + LDA approach to reproduce the 0.7-anomaly, we conclude that the formation of the magnetic impurities in the QPC might be an artifact of the LDA due to the lack of the derivative discontinuity related to the spurious self-interaction. As an indirect support of the above arguments we notice that similar spin-DFT conductance calculations (within the same LDA approach and the same parametrization of $V_{\rm xc}$) reproduce *quantitatively* the measured spin-resolved magnetoconductance of the QPCs in the integer quantum Hall regime [52]. In this case the edge state regime is reached such that the transport through the QPC corresponds to the strong coupling regime ($G_0 > 1$).

Another reason for the above discrepancy can be related to the fact that the DFT + LDA approximation might overestimate the spatial spin polarization near the smooth boundaries. Indeed, as we mentioned in section 2.2, the comparison of the DFT and the Hartree–Fock approaches shows that these two methods provide qualitatively (and in most cases quantitatively) same description of a split-gate quantum wire in the IQH regime. The most significant difference is that the DFT approximation predicts much larger spatial spin polarization near smooth boundaries at lower fields (including $B = 0$). Note that a comparative study [19] can not distinguish which approach gives a correct result. This question can be resolved by a comparison to the exact results obtained by e.g. quantum Monte Carlo methods. We speculate at this point that it is the DFT approach that overestimates the spatial spin separation at lower fields. This conclusion is based on the transport measurements on lateral quantum dots indicating that the spin-polarized injection and detection by means of the spatial separation of spins can be achieved only in the edge state regime for a sufficiently high magnetic field [4]. For the case of a QPC, the 0.5-feature in the calculated conductance (instead of the 0.7-feature observed in the experiment), is a direct consequence of the strong spatial spin polarization when one of the spin channels is completely 'repelled' from the interior of the QPC.

Based on the above discussion we conclude that while the DFT approach qualitatively captures the spontaneous spin polarization in the QPC, it however fails to reproduce quantitatively the experimentally observed 0.7-anomaly. Close to the pinch-off regime, the DFT approach predicts formation

of the spin-polarized bound states on the sides of the constriction rather than on the QPC center. Such bound states might be relevant to the experimental observation of Bird *et al* suggesting the resonance interaction between the coupled quantum point contacts close to the pinch-off regime [53]. In light of the above mentioned deficiencies of the DFT approach, it is nor clear however to what extend one can rely on the above predictions for explanations of the experimental data. We hope that our critical analysis of the standard DFT approach will stimulate further theoretical efforts that go beyond the standard DFT + LDA schemes.

3.3. Open dots

A transport regime where a sub-micron lateral structure is strongly coupled to electron reservoirs (leads) is usually referred to as an open one. This transport regime can be realized in quantum wires, dot and antidot structures typically fabricated using a split-gate or related techniques. The quantum dot operates in an open regime when the gate voltage sets up two quantum point contacts (QPCs) at the entrance and exit of the dot such that they transmit one or more channels (i.e. the conductance of an individual QPC exceeds the conductance unit $G_{\rm QPC} \gtrsim G_0 = \frac{2e^2}{h}$). In this regime electrons can freely enter and exit the dot, such that the electron number inside the dot is not integer. (Opposite regime of the Coulomb blockade corresponding to the integer electron number in the dot emerges when the point contacts are nearly pinched off). During the last decade the open quantum dots have received a significant attention providing many important insights into areas such as quantum interference, chaos, decoherence, localization and many others [54].

It is widely believed that in open transport regime as opposed to the Coulomb blockade [1] or Kondo regime [2], the electron–electron interaction plays only a minor role. We have recently revised the role of the electron–electron interaction in transport properties of open quantum dots [16, 18]. In particular, we revealed a pronounced effect of pinning of the resonant levels to the Fermi energy due to the enhanced screening. Our results represent a significant departure from a conventional picture adopted in most model Hamiltonians as well as in more sophisticated numerical calculations where a variation of external parameters (such as a gate voltage, magnetic field, etc) causes the successive dot states to sweep past the Fermi level in a linear fashion. We instead demonstrate highly nonlinear behavior of the resonant levels in the vicinity of the Fermi energy. One of the observable consequence of this effect is smearing of the conductance fluctuations. Our findings question a conventional interpretation of the ultralow temperature saturation of the coherence time in open dots which is based on the noninteracting theories where the agreement with the experiment is achieved by introducing additional phenomenological channels of dephasing. We also show that the resonant level pinning becomes especially pronounced in magnetic field. Thus, accounting for this effect might be important for the interpretation of the magnetotransport experiment in open structures, including e.g. recent studies of the electronic Mach–Zehnder interferometer [55] and the Laughlin quasi-particle interferometer [56], structures designed to test the realization of the topological quantum computing [57], antidot structures [58–60] and others. We consider an open quantum dot (figure 6) with parameters close to those studied experimentally by Huibers *et al* [61]. We consider the spinless electrons because in relatively large dots as those studied here the electrons are spin degenerate [62, 63]. We also neglect the exchange and correlation effects, which have been shown to affect the calculated conductance only marginally [16] (i.e. our calculations corresponds to the Hartree approximation).

To outline the role of quantum mechanical effects in the electron–electron interaction in open quantum dots we also consider the Thomas–Fermi (TF) approximation. In this approximation the kinetic energy is related to the electron density [8], $H_0 = \frac{\pi\hbar^2}{m^*}n(\mathbf{r})$. The self-consistent electron density is thus obtained from the solution of the equation

$$\frac{\pi\hbar^2}{m^*}n(x,y) + V_{\rm conf}(r) + V_{\rm H}(r) = E_{\rm F}. \qquad (15)$$

The electron density and the total confining potential calculated within the TF approximation do not capture quantum mechanical quantization of the electron motion. The utilization of the TF approximation for the modeling of the magnetotransport in open system is therefore conceptually equivalent to a one-electron approach. The difference between these approaches is the shape of the total confining potential: in one-electron transport simulations one typically starts with a model hard wall confinement, whereas the TF approximation gives a rather smooth potential which represents a good approximation to the actual confinement.

Figure 10(a) shows the conductance of the open quantum dot calculated in the Hartree and TF approximations (interacting and noninteracting electrons respectively) for $T = 50$ mK [18]. All the results discussed in this paper correspond to one propagating mode in the quantum point contact (QPC) openings. The striking difference between the conductance curves is clearly manifested in a strong suppression of the high frequency components of the oscillations for the interacting electrons in comparison to the noninteracting case. Thus, the electron interaction causes an apparent smearing of the conductance oscillations, which is similar to the effect of the temperature or inelastic scattering. This smearing of oscillations is caused by the pinning of resonant levels to the Fermi energy in the vicinity of resonances [16]. This is illustrated in figure 11(b) which shows an evolution of the peak position of the resonant energy levels. In the vicinity of the resonances the DOS of the dot is enhanced such that electrons with the energies close to $E_{\rm F}$ can easily screen the external potential. This leads to the 'metallic' behavior of the system when the electron density in the dot can be easily redistributed to keep the potential constant. As a result, in the vicinity of a resonance the system only weakly responds to the external perturbation (such as change of a gate voltage, magnetic field, etc), i.e. the resonant levels becomes pinned to the Fermi energy (see [16] for a detailed discussion of the pinning effect). For noninteracting electrons the nonlinear screening and hence

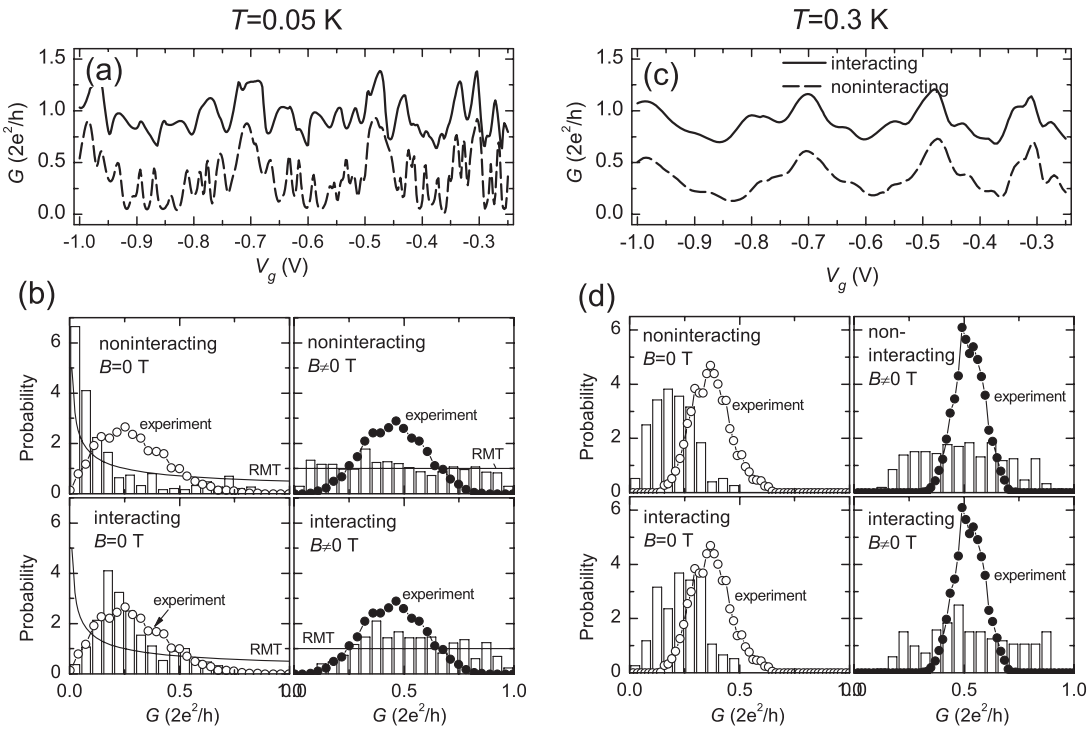

Figure 10. The calculated conductance of the open quantum dot for interacting (Hartree) and noninteracting (TF) electrons as a function of the gate voltage V_g for (a) $T = 50$ mK and (c) $T = 300$ mK; $B = 20$ mT. (The conductance curves for interacting electrons are shifted by e^2/h.) Probability distribution of the conductance $P(G)$ for interacting and noninteracting electrons for (b) $T = 50$ mK and (d) $T = 300$ mK for the cases of the time-reversed symmetry ($\beta = 1$) and the broken time-reversed symmetry ($\beta = 2$). The experimental data is adapted from [61]. Solid lines in (b), (d) correspond to the predictions of the RMT ($T = 0$, no dephasing). The layout of the gates defining the dot is similar to that one shown in figure 6. The geometrical size of the dot is 660 nm × 520 nm, the width of the leads is 540 nm. The width of the quantum point contact (QPC) openings is 100 nm (which corresponds to one propagating mode). The widths of the cap, donor and spacer layers are 14, 36 and 10 nm respectively, the donor concentration is 0.6×10^{24} m^{-3}. (Figure is adapted from [18].)

the pinning effect are absent, such that the successive dot states sweep past the Fermi level in a linear fashion, see figure 11(c).

The pinning of resonant levels drastically affects the conductance probability distribution $P(G)$. Figure 10(b) shows $P(G)$ calculated for interacting and noninteracting electrons for the cases of a time-reversal symmetry, $\beta = 1$ ($B = 0$) and a broken time-reversal symmetry, $\beta = 2$, ($B \neq 0$) for $T = 50$ mK [18]. The time-reversal symmetry is broken by application of a magnetic field $B \gtrsim \phi_0/A$, where $\phi_0 = h/e$ is the flux quantum and A is the effective dot area (typically, $B \sim 20$–40 mT). Figure 10(b) shows that the statistics of the conductance distribution $P(G)$ for the case of noninteracting electrons closely follow the corresponding random matrix theory (RMT) predictions for $\tau_\varphi = 0$ and $T = 0$ [54, 64] both for $\beta = 1$ and 2. At the same time, the statistics for the interacting electrons are strikingly different from those for the noninteracting case. Thus, due to the effect of the electron interaction, the ultralow temperature statistics of the conductance oscillations of quantum dots are not described by the RMT.

As the temperature increases, the difference between the conductances $G = G(V_g)$ as well as between the corresponding conductance distributions $P(G)$ for interacting and noninteracting electrons diminishes, and for a sufficiently high temperature this difference disappears, see figures 10 (c) and (d) ($T = 300$ mK). The reason for that is that the temperature strongly reduces the effect of resonant level pinning. Indeed, when the transport energy window, $\sim 2\pi k_B T$, (determined by the condition when the derivative of the Fermi–Dirac distribution is distinct from zero exceeds the mean-level spacing $\Delta = \frac{2\pi\hbar^2}{m*A}$), the conductance is mediated by several levels. As a result, several levels always contribute to screening at the same time and hence the screening efficiency of the dot is affected very little when a gate voltage or magnetic field are varied. Note that for the dot under consideration the condition $2\pi k_B T = \Delta$ corresponds to $T \approx 100$ mK. Thus, for $2\pi k_B T \gtrsim \Delta$ the effect of the electron interaction on the conductance is strongly suppressed, and therefore the conductance and their probability distributions for interacting and noninteracting electrons are practically the same.

The probability distribution $P(G)$ in open quantum dots with one propagating channel in the leads was studied by Huiberts *et al* [61]. Figure 10(b) shows that in the regime of the ultralow temperatures, $T = 50$ mK, the calculated conductance statistics for interacting electrons agree quite well with the corresponding experimental distribution $P(G)$ both for $\beta = 1$ and 2. The measured conductance distribution $P(G)$ in [61] was well described by the RMT predictions where the inelastic scattering was introduced using τ_φ as a fitting parameter. Our results, instead, demonstrate that once the electron interaction is accounted for, the agreement with the experiment for $2\pi k_B T \lesssim \Delta$ is achieved without assuming additional inelastic scattering

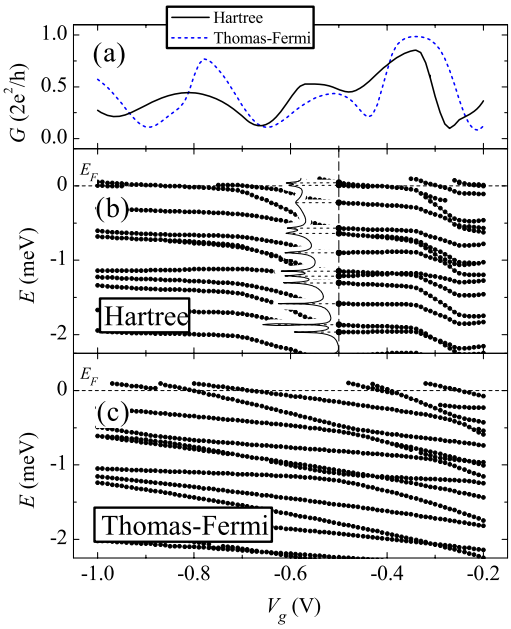

Figure 11. The conductance (a) and the resonant energy structure of the open quantum dot calculated within the Hartree (b) and Thomas–Fermi approximations (c) (interacting and noninteracting electrons respectively). Inset in (b) shows the density of states (DOS) for $V_g = -0.5$ V. The layout of the gates and parameters of the heterostructure are similar to those of figure 10; $T = 0.2$ K. (Figure is adapted from [16]).

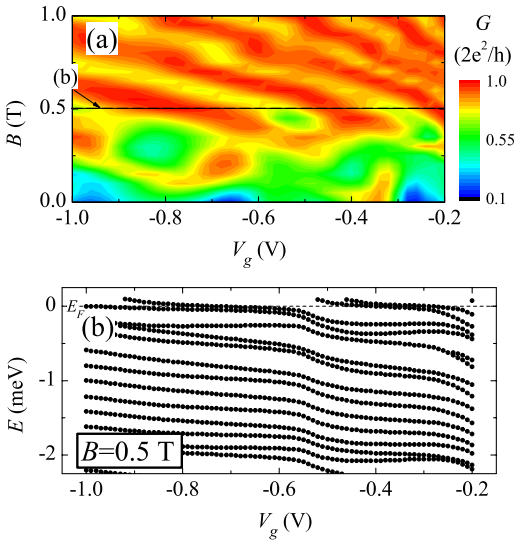

Figure 12. (a) The conductance of the open quantum dot as a function of the magnetic field B and gate voltage V_g calculated within the Hartree approximation. (b) The energy structure for $B = 0.5$ T calculated within the Hartree approximation. The layout of the gates and parameters of the heterostructure are similar to those of figure 10; $T = 0.2$ K. (Figure is adapted from [16].)

channels. We thus conclude that for the regime of ultralow temperatures the experimentally inferred value of τ_φ might be greatly underestimated which implies that the dephasing time does not saturate. As the temperature increases, the calculated conductance distribution starts to deviate from the experimental statistics, see figure 10(d). As discussed above, for the temperature $2\pi k_B T \gtrsim \Delta$ the electron interaction practically does not affect the conductance oscillations and their statistics. Thus, for $2\pi k_B T \gtrsim \Delta$ the difference between the calculated and experimental statistics can be attributed to the effect of dephasing. Our criterion for the transition temperature $2\pi k_B T \sim \Delta$ is consistent with the findings reported by Bird *et al* [65, 66] and Clarke *et al* [67] who find a saturation behavior of τ_φ at the transition temperatures T_{onset} near the mean-level spacing. A relation between T_{onset} and Δ was also discussed by Hackens *et al* [68]. However, some experiments [69] do not show a clear relation between T_{onset} and Δ, such that more systematic studies are needed in order to prove the connection between T_{onset} and Δ.

Pinning of the resonant levels in open dots discussed above becomes much more pronounced in sufficiently high magnetic field when the electron transport is mediated by the edge states with a characteristic dimension of the order of the magnetic length $l_B = \sqrt{\hbar/eB}$. In the edge state transport regime the backscattering on the potential defining the quantum dot decreases and, for a large enough B, electrons pass through the device with the transmission close to unity. Transport in such a regime is referred to as adiabatic. For the open quantum dot under study, transition to adiabatic propagation takes place at about $B \approx 0.5$ T, see figure 12(a). The conductance for $B \gtrsim 0.5$ T shows pronounced oscillations due to the Aharonov–Bohm interference. When the magnetic field changes such that the total magnetic flux $\Phi = BS$ through the dot modifies by the one flux quantum $\phi_0 = h/e$, the conductance demonstrates periodic oscillations with the period $\Delta B = \phi_0/S$ (S is the characteristic area of the dot). Using the actual dot area S_a we get $\Delta B = 0.11$ T, which is nearly twice less than extracted from figure 12(a), where $\Delta B = 0.25$ T. The discrepancy can be related to a finite extent of the edge state circulating inside the dot ($l_B \approx 35$ nm for $B = 0.5$). As a result, the area enclosed by the edge state is much smaller than the geometrical area of the dot.

The resonant energy structure is modified substantially when a magnetic field is applied, cf figure 12(b) for $B = 0.5$ T and figure 11(b) for $B = 0$ T. The resonant levels exhibit almost equal separation which can be related to the well-known Darwin–Fock-type energy spectrum formation for the corresponding closed dot [23, 70]. The distinguished feature of the energy level structure is much stronger pinning of the resonant levels to E_F that persists over larger intervals of V_g in comparison to the $B = 0$ case. Stronger pinning can be attributed to the enhanced screening efficiency because of the increased localization of the wavefunction for the case of nonzero magnetic field. As we mentioned in the beginning of this section the strong pinning of the resonant energy levels in the presence of the magnetic field can have a profound effect on transport properties of various devices operating in the edge state transport regime including the Mach–Zehnder [55] and the Laughlin [56] interferometers as well as antidot devices [57–60]. It is worth mentioning that another manifestation of the pinning in the edge state regime is the well-known effect of formation of the compressible and incompressible strips near the structure boundary discussed in section 2.2.

The findings reported in this section outline the importance of the first-principle self-consistent quantum transport calculations for open quantum dots. Indeed, accounting for both global electrostatics through the Hartree potential and the quantum mechanical quantization in a self-consistent way is essential for revealing of the pinning effect that causes a drastic difference in the conductance of the interacting and noninteracting electrons. Note that this effect would not be captured in approaches utilizing model Hamiltonians where the electron interaction is accounted thought the classical capacitance charging.

4. Conclusion

We have developed a mean-field approach to study electronic and transport properties of various low dimensional lateral structures, including quantum wires, quantum antidots, quantum point contacts and open quantum dots [11–19]. The electron interactions and spin effects are included within the spin density functional theory in the local density approximation where the conductance, the effective potentials, the band structure are calculated on the basis of the Green's function technique. The developed approach corresponds to the first-principles magnetoconductance calculation (within the effective mass approximation), that starts from a geometrical layout of the device and is free from phenomenological parameters of the theory. The strength of the present approach is that it can provide a detailed microscopic information about electron densities, wavefunctions, potentials, etc. This is not always possible within approaches relying on model Hamiltonians containing phenomenological parameters such as coupling strengths or charging constants. In many cases it is not always straightforward to relate quantitatively the above parameters to the physical processes they represent in the real system and sometimes it is not even obvious whether a model description is sufficient to capture the essential physics. At the same time, the DFT approach can deal with large realistic systems containing hundreds or thousands of electrons. Such systems would be forbiddingly large for exact methods such as quantum Monte Carlo or configurational integration. We have applied the present approach to study the energetics, spin polarization, effective g factor, magnetosubband and edge state structure of split-gate and cleaved-edge overgrown quantum wires as well as to calculate a conductance of quantum point contacts and open quantum dots. In the present paper we present a systematic review of the major obtained results.

Electronic, spin, and edge state structure of the split-gate quantum wires and antidots. We provide a quantitative description of the structure of edge states in split-gate quantum wires in the integer quantum Hall regime [11, 12, 15, 19]. We discuss how the spin-resolved subband structure, the current densities, the confining potentials, as well as the spin polarization of the electron and current densities evolve when an applied magnetic field varies. We demonstrate that the exchange and correlation interactions dramatically affect the magnetosubbands in quantum wires bringing about qualitatively new features in comparison to a widely used Chklovskii *et al* [6] model of spinless edge states [6]. In particular, we demonstrate that the exchange interaction can completely suppress the formation of the compressible strips and lead to a spatial spin polarization of the edge states. We also discuss the energetics and the edge state structure of the quantum antidot and compare them with the corresponding results for the split-gate quantum wire [14].

Electronic, spin, and edge state structure of the cleaved-edge overgrown quantum wires. We provide a systematic quantitative description of the structure of edge states and magnetosubband evolution in cleaved-edge quantum wires with a hard wall confinement in the integer quantum Hall regime [13]. We show that they exhibit different features as compared to the case of a smooth confinement in the split-gate wires. In particular, in the hard wall wires a deep and narrow triangular potential well of the width of the magnetic length is formed in the vicinity of the wire boundary. The wavefunctions are strongly localized in this well, which leads to an increase of the electron density near the edges. In contrast to the case of a smooth confinement, in the hard wall wires compressible strips do not form in the vicinity of the wire boundaries and a spatial spin separation between spin-up and spin-down states near edges is absent.

We stress that we focused on quantum wires and antidot structures in the integer quantum Hall regime. It is also possible to extend present analysis (both for the split-gate and cleaved-edge overgrown quantum wires as well as the antidots) to the fractional regime. This requires a proper description of the exchange and correlations at fractional fillings. (Various recipes for the parametrization of the exchange and correlation potential within the framework of the DFT in the regime of strong fields $\nu < 1$ are reviewed in [7] and [51].) The strong correlations at fractional filling causes the discontinuity cups in the full exchange–correlation energy [71, 72] which is shown to lead to the appearance of incompressible strips at the edges at fractional filling factors [71]. An extension of the present methods into fractional Hall regime (which remains to be developed) would undoubtedly provide new microscopical insight into the systems at hand.

Conductance and 0.7-anomaly in quantum point contacts. We studied the role of the electron interaction and spin effects in transport properties of quantum point contacts [17]. In particular, we show that both short and long QPCs show the pronounced plateau-like feature in the conductance at $\sim 0.5 \times 2e^2/h$. On the contrary, the experimental data clearly show an anomaly in the conductance around $0.7 \times 2e^2/h$. Therefore, while the spin-DFT-based 'first-principle' calculations predict the spin polarization in the QPC structure, the calculated conductance clearly does not reproduce the 0.7-anomaly observed in almost all QPCs of various geometries. (It should be stressed that the calculated 0.5 plateau corresponds to the complete suppression of one spin channel, whereas experimentally observed 0.7-anomaly means that both spin channels are present in the conductance). We have critically examined the obtained results and argue that the inability of the DFT approach to reproduce quantitatively the 0.7-anomaly may be due to the uncorrected self-interaction errors in the DFT transport calculation (related to the derivative

discontinuity in the exchange–correlation potential V_{xc} [8]) for the case when localization of charge is expected to occur, so that the magnetic impurity formation may be an artifact of the DFT due to the spurious self-interaction. Our results thus outline the need for further theoretical studies of the QPC conductance based on the approaches that go beyond the standard DFT + LDA scheme and that account for the derivative discontinuity in the V_{xc} or utilize similar corrective schemes eliminating the self-interaction errors of the DFT + LDA. Another reason for not recovering of the 0.7-anomaly can be related to the fact that the DFT + LDA approximation might overestimate the spatial spin polarization near the smooth boundaries. This conclusion follows from a comparison of the DFT and Hartree–Fock calculations for the quantum wire [19]. Thus, further studies of quantum wires based on the exact approaches (e.g. quantum Monte Carlo, etc) are needed in order to resolve this issue.

Effect of electron interaction in open quantum dots. We have revised the role of the electron–electron interaction in transport properties of open quantum dots. In particular, we revealed a pronounced effect of pinning of the resonant levels to the Fermi energy due to the enhanced screening [16]. Our results represent a significant departure from a conventional picture adopted in most model Hamiltonians as well as in more sophisticated numerical calculations where a variation of external parameters (such as a gate voltage, magnetic field, etc) causes the successive dot states to sweep past the Fermi level in a linear fashion. We instead demonstrate highly nonlinear behavior of the resonant levels in the vicinity of the Fermi energy. One of the observable consequence of this effect is smearing of the conductance fluctuations. We also show that the resonant level pinning becomes especially pronounced in magnetic field. Thus, accounting for this effect might be important for the interpretation of the magnetotransport experiment in open structures, including e.g. recent studies of the electronic Mach–Zehnder interferometer [55] and the Laughlin quasi-particle interferometer [56], structures designed to test the realization of the topological quantum computing [57], antidot structures [58–60] and others. We also demonstrate that in the regime of the ultralow temperatures $2\pi k_B T \lesssim \Delta$ (Δ being the mean-level spacing), the electron interactions strongly smears the conductance oscillations and thus significantly affects their statistics. Our calculations are in good quantitative agreement with the observed ultralow temperature statistics of Huibers *et al*. Our findings question a conventional interpretation of the ultralow temperature saturation of the coherence time in open dots which is based on the noninteracting theories where the agreement with the experiment is achieved by introducing additional phenomenological channels of dephasing [18].

We finally note that a developed theoretical approach for conductance calculation in open systems is limited to the case of the strong coupling ($G > G_0$) as well as to the integer quantum Hall (IQH) regime (filling factor $\nu > 1$). First-principles description of weakly coupled IQH systems as well as the fractional quantum Hall systems (both in the weak and strong coupling regimes) has not been reported yet and still represents a challenge to the theory.

Acknowledgment

The numerical calculations were performed in part using the facilities of the National Supercomputer Center, Linköping, Sweden.

References

[1] Beenakker C W J and van Houten H 1991 *Solid State Physics: Advances in Research and Applications* vol 44 (San Diego, CA: Academic)
[2] Kastner M and Goldhaber-Gordon D 2001 *Solid State Commun.* **119** 245
[3] Ando T, Fowler A B and Stern F 1982 *Rev. Mod. Phys.* **54** 437
[4] Ciorga M, Pioro-Ladriere M, Zawadzki P, Hawrylak P and Sachrajda S A 2002 *Appl. Phys. Lett.* **80** 2177
[5] Thomas K J, Nicholls J T, Simmons M Y, Pepper M, Mace D R and Ritchie D A 1996 *Phys. Rev. Lett.* **77** 135
[6] Chklovskii D B, Shklovskii B I and Glazman L I 1992 *Phys. Rev.* B **46** 4026
[7] Reimann S M and Manninen M 2002 *Rev. Mod. Phys.* **74** 1283
[8] Giuliani G F and Vignale G 2005 *Quantum Theory of the Electron Liquid* (Cambridge: Cambridge University Press)
[9] Davies J H, Larkin I A and Sukhorukov E V 1995 *J. Appl. Phys.* **77** 4504
[10] Martorell J, Wu H and Sprung D W L 1994 *Phys. Rev.* B **50** 17298
[11] Ihnatsenka S and Zozoulenko I V 2006 *Phys. Rev.* B **73** 075331
[12] Ihnatsenka S and Zozoulenko I V 2006 *Phys. Rev.* B **73** 155314
[13] Ihnatsenka S and Zozoulenko I V 2006 *Phys Rev.* B **74** 075320
[14] Ihnatsenka S and Zozoulenko I V 2006 *Phys. Rev.* B **74** 201303(R)
[15] Ihnatsenka S and Zozoulenko I V 2007 *Phys. Rev.* B **75** 035318
[16] Ihnatsenka S, Zozoulenko I V and Willander M 2007 *Phys. Rev.* B **75** 235307
[17] Ihnatsenka S and Zozoulenko I V 2007 *Phys. Rev.* B **76** 045338
See also Ihnatsenka S and Zozoulenko I V 2007 *Preprint* cond-mat/0701657v1 [cond-mat.mes-hall] unpublished
[18] Ihnatsenka S and Zozoulenko I V 2007 *Phys. Rev. Lett.* **99** 166801
[19] Ihnatsenka S and Zozoulenko I V 2007 submitted (Ihnatsenka S and Zozoulenko I V 2007 *Preprint* 0707.0126v1 [cond-mat.mes-hall])
[20] Tanatar B and Ceperley D M 1989 *Phys. Rev.* B **39** 5005
[21] Attacalite C, Moroni S, Gori-Giorgi P and Bachelet G B 2002 *Phys. Rev. Lett.* **88** 256601
[22] Datta S 1997 *Electronic Transport in Mesoscopic Systems* (Cambridge: Cambridge University Press)
[23] Davies J 1998 *The Physics of Low-Dimensional Semiconductors* (Cambridge: Cambridge University Press)
[24] Singh D, Krakauer H and Wang C S 1986 *Phys. Rev.* B **34** 8391
[25] Suzuki T and Ando T 1993 *J. Phys. Soc. Japan* **62** 2986
Suzuki T and Ando T 1998 *Physica* B **249–251** 415
[26] Oto K, Takaoka S and Murase K 2001 *Physica* B **298** 18
[27] Pfeiffer L N, West K W, Eisenstein H L, Baldwin K W, Gershoni D and Spector J 1990 *Appl. Phys. Lett.* **56** 1697
[28] Grayson M 2006 *Solid State Commun.* **140** 66
[29] Huber M, Grayson M, Rother M, Biberacher W, Wegscheider W and Abstreiter G 2005 *Phys. Rev. Lett.* **94** 016805
[30] Zozoulenko I V, Maaø F A and Hauge E H 1996 *Phys. Rev.* B **53** 7975
Zozoulenko I V, Maaø F A and Hauge E H 1996 *Phys. Rev.* B **53** 7987
[31] Lang N D 1995 *Phys. Rev.* B **52** 5335
[32] Taylor J, Guo H and Wang J 2001 *Phys. Rev.* B **63** 245407
[33] Damle P S, Ghosh A W and Datta S 2001 *Phys. Rev.* B **64** 201403(R)

[34] Evers F, Weigend F and Koentopp M 2004 *Phys. Rev.* B **69** 235411
[35] Toher C, Filippetti A, Sanvito S and Burke K 2005 *Phys. Rev. Lett.* **95** 146402
[36] Koentopp M, Burke K and Evers F 2006 *Phys. Rev.* B **73** 121403(R)
[37] Palacios J J 2005 *Phys. Rev.* B **72** 125424
[38] Stefanucci G and Almbladh C-O 2004 *Phys. Rev.* B **69** 195318
[39] Zheng X and Chen G H 2005 *Preprint* physics/0502021
[40] Ferretti A, Calzolari A, Di Felice R and Manghi F 2005 *Phys. Rev.* B **72** 125114
[41] Wang C-K and Berggren K-F 1998 *Phys. Rev.* B **57** 4552
[42] Berggren K-F and Yakimenko I I 2002 *Phys. Rev.* B **66** 085323
[43] Starikov A A, Yakimenko I I and Berggren K-F 2003 *Phys. Rev.* B **67** 235319
Jaksch P, Yakimenko I I and Berggren K-F 2006 *Phys. Rev.* B **74** 235320
[44] Havu P, Puska M J, Nieminen R M and Havu V 2004 *Phys. Rev.* B **70** 233308
[45] Hirose K, Meir Y and Wingreen N S 2003 *Phys. Rev. Lett.* **90** 026804
[46] Rejec T and Meir Y 2006 *Nature* **442** 900
[47] Thomas K J, Nicholls J T, Simmons M Y, Pepper M, Mace D R and Ritchie D A 1996 *Phys. Rev. Lett.* **77** 135
[48] Thomas K J, Nicholls J T, Appleyard N J, Simmons M Y, Pepper M, Mace D R, Tribe W R and Ritchie D A 1998 *Phys. Rev.* B **58** 4846
[49] Reilly D J 2005 *Phys. Rev.* B **72** 033309
[50] Rokhinson L P, Pfeiffer L N and West K W 2006 *Phys. Rev. Lett.* **96** 156602
[51] See e.g. Saarikoski H, Räsäänen E, Siljamäaki S, Harju A, Puska M J and Nieminen R M 2003 *Phys. Rev.* B **67** 205327
[52] Radu I P, Miller J B, Amasha S, Levenson-Falk E, Zumbuhl D M, Kastner M A, Marcus C M, Pfeiffer L N and West K W 2008 unpublished
Ihnatsenka S and Zozoulenko I V 2008 *Preprint* 0801.1820v1 [cond-mat.mes-hall]
[53] Morimoto T, Iwase Y, Aoki N, Sasaki T, Ochiai Y, Shailos A, Bird J P, Lilly M P, Reno J L and Simmons J A 2003 *Appl. Phys. Lett.* **82** 3952
Bird J P and Ochiai Y 2004 *Science* **303** 1621
Yoon Y, Mourokh L, Morimoto T, Aoki N, Ochiai Y, Reno J L and Bird J P 2007 *Phys. Rev. Lett.* **99** 136805
[54] For a review, see, e.g. Beenakker C W J 1997 *Rev. Mod. Phys.* **69** 731
Alhassid Y 2000 *Rev. Mod. Phys.* **72** 895
[55] Ji Y, Chung Y, Sprinzak D, Heiblum M, Mahalu D and Shtrikman H 2003 *Nature* **422** 415
[56] Camino F E, Zhou W and Goldman V J 2005 *Phys. Rev.* B **72** 075342
[57] See e.g. Das Sarma S, Freedman M and Nayak C 2006 *Phys. Today* **59** 32 and references therein
[58] Ford C J B, Simpson P J, Zailer I, Mace D R, Yosefin M, Pepper M, Ritchie D A, Frost J E F, Grimshaw M P and Jones G A C 1994 *Phys. Rev.* B **49** 17456
Kataoka M, Ford C J B, Faini G, Mailly D, Simmons M Y and Ritchie D A 2000 *Phys. Rev.* B **62** R4817
[59] Karakurt I, Goldman V J, Liu J and Zaslavsky A 2001 *Phys. Rev. Lett.* **87** 146801
Kataoka M and Ford C J B 2004 *Phys. Rev. Lett.* **92** 199703
Goldman V J 2004 *Phys. Rev. Lett.* **92** 199704
[60] Zozoulenko I V and Evaldsson M 2004 *Appl. Phys. Lett.* **85** 3136
[61] Huibers A G, Patel S R, Marcus C M, Brouwer P W, Duruöz C I and Harris J S Jr 1998 *Phys. Rev. Lett.* **81** 1917
[62] Folk J A, Patel S R, Birnbaum K M, Marcus C M, Duruöz C I and Harris J S Jr 2001 *Phys. Rev. Lett.* **86** 2102
[63] Evaldsson M, Zozoulenko I V, Ciorga M, Zawadzki P and Sachrajda A S 2004 *Europhys. Lett.* **68** 261
Evaldsson M and Zozoulenko I V 2006 *Phys. Rev.* B **73** 035319
[64] Baranger H U and Mello P A 1994 *Phys. Rev. Lett.* **73** 142
Jalabert R A, Pichard J-L and Beenakker C W 1994 *Europhys. Lett.* **27** 255
[65] Bird J P, Ishibashi K, Ferry D K, Ochiai Y, Aoyagi Y and Sugano T 1995 *Phys. Rev.* B **51** 18037
[66] Pivin D P Jr, Andresen A, Bird J P and Ferry D K 1999 *Phys. Rev. Lett.* **82** 4687
[67] Clarke R M, Chan I H, Marcus C M, Duruöz C I, Harris J S Jr, Campman K and Gossard A C 1995 *Phys. Rev.* B **52** 2656
[68] Hackens B, Faniel S, Gustin C, Wallart X, Bollaert S, Cappy A and Bayot V 2005 *Phys. Rev. Lett.* **94** 146802
[69] Huibers A G, Folk J A, Patel S R, Marcus C M, Duruöz C I and Harris J S Jr 1999 *Phys. Rev. Lett.* **83** 5090
[70] Zozoulenko I V, Sachrajda A S, Gould C, Berggren K-F, Zawadzki P, Feng Y and Wasilewski Z 1999 *Phys. Rev. Lett.* **83** 1838
[71] Heinonen O, Lubin M I and Johnson M D 1995 *Phys. Rev. Lett.* **75** 4110
Ferconi M, Geller M R and Vignale G 1995 *Phys. Rev.* B **52** 16357
[72] Price R and Das Sarma S 1996 *Phys. Rev.* B **54** 8033